Chinese Chemical Letters 36 (2025) 109984

Contents lists available at ScienceDirect

Chinese Chemical Letters

journal homepage: www.elsevier.com/locate/cclet

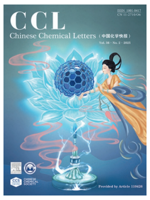

Novel 3D-on-2D g-C_3N_4/$AgIn_xS_y$ heterojunction photocatalyst for simultaneous and stoichiometric production of H_2 and H_2O_2 from water splitting under visible light

Hualin Jiang[a], Wenxi Ye[a], Huitao Zhen[a], Xubiao Luo[a,b], Vyacheslav Fominski[c], Long Ye[a,*], Pinghua Chen[a,*]

[a] Key Laboratory of Jiangxi Province for Persistent Pollutants Control and Resources Recycle, Nanchang Hangkong University, Nanchang 330063, China
[b] College of life science, Jinggangshan University, Ji'an 343009, China
[c] National Research Nuclear University MEPhI (Moscow Engineering Physics Institute), Moscow 115409, Russia

ARTICLE INFO

Article history:
Received 24 December 2023
Revised 8 April 2024
Accepted 8 May 2024
Available online 9 May 2024

Keywords:
Photocatalysis
Water splitting
g-C_3N_4
Silver indium sulfide
H_2 production
H_2O_2 production

ABSTRACT

Photocatalytic H_2 production from water splitting is a promising candidate for solving the increasing energy crisis and environmental issues. Herein we report a novel g-C_3N_4/$AgIn_xS_y$ S-scheme heterojunction photocatalyst for water splitting into stoichiometric H_2 and H_2O_2 under visible light. The catalyst was prepared by depositing 3D bimetallic sulfide ($AgIn_xS_y$) nanotubes onto 2D g-C_3N_4 nanosheets. Owing to the special 3D-on-2D configuration, the photogenerated carriers could be rapidly transferred and effectively separated through the abundant interfacial heterostructures to avoid recombination, and therefore excellent performance for visible light-driven water splitting could be obtained, with a 24-h H_2 evolution rate up to 237 μmol g^{-1} h^{-1}. Furthermore, suitable band alignment enables simultaneous H_2 and H_2O_2 production in a 1:1 stoichiometric ratio. H_2 and H_2O_2 were evolved on the conduction band of g-C_3N_4 and on the valance band of $AgIn_xS_y$, respectively. The novel 3D-on-2D configuration for heterojunction construction proposed in this work provided alternative research ideas toward photocatalytic reaction.

Nowadays, global energy crisis and environmental issues have become an imminent threat to human development. Solar-driven overall water splitting into H_2 and O_2 under photocatalysts is considered as the ultimate approach towards solar-to-fuel conversion [1-5], due to the carbon-free feature, simple facilities, as well as low cost [6-8]. However, this strategy has an inherent defect where the evolved gaseous H_2 and O_2 mixture needs to be separated for safe application [9,10]. Moreover, direct oxidation reaction of H_2O to O_2 was demonstrated to suffer from slow kinetics due to the complicated four-electron pathway [11]. One feasible strategy to address these problems is to avoid O_2 evolution by adding hole scavengers [12], but the resulting complicated operation and maintenance process along with the high cost of sacrificial reagents make this strategy not very progressive indeed. Another alternative solution is to split water into H_2 and H_2O_2, in which the reaction proceeds in a two-electron pathway (*i.e.*, $2H_2O \rightarrow H_2 + H_2O_2$). Although the four-electron pathway for O_2 evolution is thermodynamically more favored than two-electron pathway for H_2O_2 production (1.23 eV *vs.* 1.78 eV), the latter was demonstrated to be faster in kinetics [13-15]. The water-soluble H_2O_2 product avoids the gas separation process after water splitting. Additionally, H_2O_2 itself can be served as high-value oxidant with widespread application in food, medicine, industry and daily life. In industry, H_2O_2 is currently produced through an energy-intensive anthraquinone process [16]. Therefore, simultaneous H_2 and H_2O_2 production from photocatalytic water splitting provides an appealing alternative to solar-to-fuel and solar-to-oxidant conversion [17].

The design and fabrication of efficient, stable, and low-cost photocatalysts is the core issue for photocatalytic water splitting. Since the pioneer works of Fujishima [18,19], semiconductor materials have been intensively investigated as photocatalysts for water splitting. Among them, graphitic carbon nitride (g-C_3N_4) was the first reported material for photocatalytic H_2 production from water splitting under visible light [20]. The past decade has witnessed the rapid development of g-C_3N_4-based photocatalysts for overall water splitting, due to their simple preparation method, superior chemical stability, resistance to photocorrosion, and appropriate band structure for water splitting [21-25]. g-C_3N_4 was also capable of catalyzing water splitting to produce H_2O_2 [13-15].

---

* Corresponding authors.
E-mail addresses: yelong@nchu.edu.cn (L. Ye), cph1979@126.com (P. Chen).

https://doi.org/10.1016/j.cclet.2024.109984

Unfortunately, the intrinsically poor conductivity, rapid recombination of photogenerated carriers and the inactive surface limit its practical application [26-28]. Various strategies have been adopted to address these problems, such as doping, defect engineering, and heterojunction construction [14,29-30]. Integration of functionalized cocatalyst with g-C_3N_4 primary catalyst to construct heterostructures in their interfacial region holds tremendous promise in terms of both enhanced charge separation and surface activation [31]. The intimate contact between cocatalyst and g-C_3N_4 is an essential requirement to induce vertical migration of photogenerated carriers to active sites [26,32]. For instance, Xue *et al.* [30] constructed a novel [P-doped g-C_3N_4]/[red phosphorus]/[Co_xP] heterojunction photocatalyst for water splitting. It was confirmed that electron transfer *via* homogeneous phosphorus bridges in interfacial regions enabling boosted photocatalytic generation of H_2 and H_2O_2. Similar result was also observed in [P-doped g-C_3N_4]/[Co_xNi_yP] heterojunction photocatalyst, in which the chemical connection between primary and cocatalyst *via* a $P^{+}-P^{\delta-}-Co^{\delta+}/Ni^{\delta+}$ bridge endowed the photocatalyst with an excellent H_2 evolution rate as high as 239.3 μmol g^{-1} h^{-1} [31]. It is also worth noting that the size and distribution of a given cocatalyst need to be refined to provide more active sites for catalysis [31,33]. However, it usually becomes failure when researchers strive to simultaneously impart the aforementioned properties to one photocatalytic system. A readily producible, efficient, stable, and low-cost catalyst with broadband photocatalytic performance for H_2 and H_2O_2 production from water splitting is thus highly desirable.

Herein, we report a novel g-C_3N_4/$AgIn_xS_y$ heterojunction photocatalyst for the simultaneous production of H_2 and H_2O_2 from water splitting. The composite catalyst was prepared by classic thermal polycondensation method followed by simple coprecipitation process. Bimetallic sulfide was selected as the cocatalyst in view of its low cost, intensive visible-light response and widespread application in optical, optoelectronic, and photocatalytic areas [34-37]. Especially, the tubular $AgIn_xS_y$ deposited on the g-C_3N_4 nanosheet is expected to construct a robust 3D-on-2D configuration for a more abundant interfacial heterostructures. Spectroscopic and photoelectrochemical studies were performed to disclose the interfacial charge transfer behavior between primary and cocatalyst. The photocatalytic performance for water splitting was evaluated under visible irradiation ($\lambda > 420$ nm) to reveal the simultaneous and stoichiometric feature of H_2 and H_2O_2 production. And finally, a reasonable photocatalytic mechanism for water splitting into H_2 and H_2O_2 was proposed according to the results of active sites and band alignment analyses. g-C_3N_4 nanosheets were prepared by thermal polycondensation of melamine precursor followed by a further thermal exfoliation process (see Supporting information for detailed preparation and characterization methods). g-C_3N_4/$AgIn_xS_y$ composite photocatalysts were prepared by the coprecipitation method. The pristine g-C_3N_4 nanosheets (g-C_3N_4) showed a blocky morphology with relatively flat surface (Fig. 1a) ascribed to the insufficient exfoliation of nanosheets and resultant interlayer stacking. The morphology of pristine silver indium sulfide (AIS) was considered as an aggregate of many randomly arranged nanotubes with an outer diameter of 30–50 nm and an inner diameter of 10–20 nm (Fig. 1b), respectively. AIS nanotubes were not very uniform in diameter and length. After coprecipitation reaction, many nanorods were deposited onto the flat g-C_3N_4 surface (Figs. 1c and d). The diameters of these nanorods were roughly equal to the outer diameter of pristine AIS nanotubes.

TEM images of the composite verified the tubular structure of the deposited nanorods (Fig. 1e). The inner diameter of the deposited nanotubes was also comparable to that of pristine AIS nanotubes, indicating the g-C_3N_4 component in a coprecipitation deposition process had negligible influence on the formation and structure of AIS nanotubes. The element mapping images of the composite showed a uniform distribution of C and N elements on the surface of the material, while the distribution of Ag, In and S elements was consistent with the position of nanotubes (Fig. S1 in Supporting information). The composition of g-C_3N_4/AIS composite was further investigated by high-resolution TEM. As shown in Fig. 1f, the lattice fringes, with spacings of 0.33, 0.31 and 0.19 nm, were clearly observed in the nanotube region, corresponding to the (002), (201) lattice planes of $AgInS_2$ and (440) plane of $AgIn_5S_8$ [38], respectively. Furthermore, lattice fringe with spacing of 0.32 nm was also observed in the flat region, corresponding to the (002) plane of g-C_3N_4. All the above analyses proved that we have successfully prepared g-C_3N_4 nanosheets/AIS nanotubes composite.

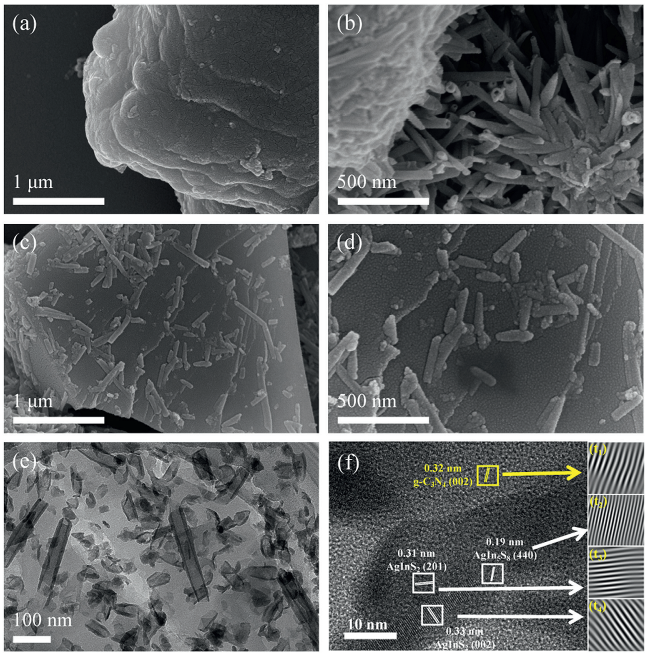

Fig. 1. SEM micrographs of g-C_3N_4 (a), AIS (b), and 70-GAIS (c, d). (e) TEM and (f) HRTEM micrographs of 70-GAIS. t_1, t_2, t_3 and t_4 display the inverse fast Fourier transform (IFFT) corresponding to the related regions.

The crystalline structure of the composite was further investigated by X-ray diffraction analysis. As shown in Fig. 2a, g-C_3N_4 gave two characteristic peaks at 12.9° and 27.6°, corresponding to (100) and (002) lattice planes, respectively. The former is attributed to the in-planar repeating triazine motifs while the latter originates from the interlayer stacking of g-C_3N_4 sheets [39,40]. For AIS nanotubes, the diffraction peaks appeared at 25.4°, 26.6°, 28.4°, 28.7°, 44.5°, 52.6°, 13.2° and 47.3°, where the first six peaks were aroused by the (200), (002), (121), (201), (320) and (322) planes of $AgInS_2$ (PDF #25–1328) while the last two peaks were attributed to the (111) and (440) planes of $AgIn_5S_8$ (PDF #25–1029) [38]. The aforementioned diffraction peaks were all observed in the pattern of the g-C_3N_4/AIS composite.

To reveal the surface chemical composition and state of the g-C_3N_4/AIS photocatalyst, X-ray photoelectron spectroscopy (XPS) characterization was then performed. All binding energies were calibrated by C 1s binding energy at 284.6 eV. As anticipated, various element signals reasonably appeared in the spectra of corresponding samples (Fig. 2b). Note that a C 1s signal was also observed in the spectrum of AIS. Since AIS is a carbon-free material, this C 1s signal could be attribute to C–C from adventitious carbon contaminant. The deconvoluted C 1s high-resolution XPS

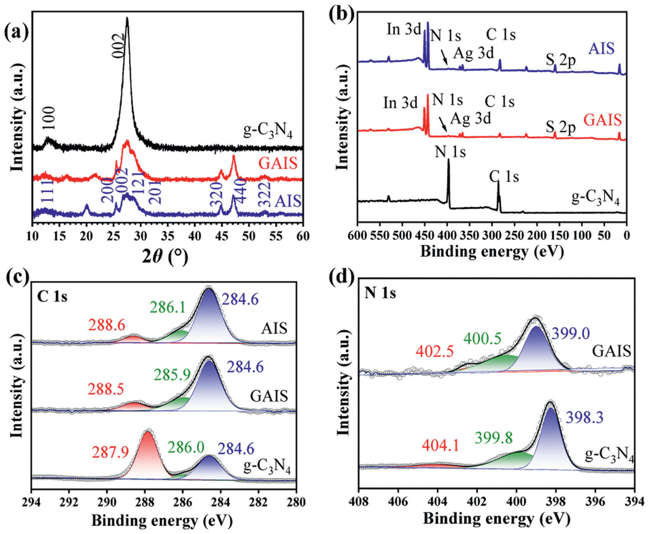

Fig. 2. XRD patterns (a), XPS spectra (b), and C 1s high-resolution XPS spectra (c) of g-C_3N_4, AIS, and 70-GAIS. (d) N 1s high-resolution XPS spectra of g-C_3N_4 and 70-GAIS.

peaks of g-C_3N_4 and GAIS at 287.9 and 288.6 eV could be assigned to the sp^2-hybridized carbon (N=C−(N)$_2$, see Fig. 2c) [41]. In N 1s XPS spectrum of g-C_3N_4, the peak at 398.3 eV was assigned to the sp^2-hybridized nitrogen (C=N−C), the peak at 399.8 eV to the three-coordinate nitrogen (N−(C)$_3$), and the peak at 404.1 eV to the π-excitation of C−N heterocycles (Fig. 2d) [42]. The spectrum of GAIS showed similar N species whereas the peaks were located at 399.0, 400.5, and 402.5 eV, respectively. The significant positive shift (+0.7 eV) of the N 1s binding energy for both C=N−C and N−(C)$_3$ groups, indicating a decreased N electron density, could be caused by the electron transfer from g-C_3N_4 to AIS at the interfacial region [42,43]. This argument can be further validated by high-resolution XPS spectra of other elements (Fig. S2 in Supporting information). As shown in Fig. S2a, AIS displayed two Ag 3d peaks centered at 373.9 and 368.0 eV, which can be assigned to Ag $3d_{3/2}$ and Ag $3d_{5/2}$ core levels [44,45]. For GAIS, these two peaks shifted to 373.8 and 367.8 eV respectively, suggesting slight increasing of Ag electron density in AIS component after being deposited on g-C_3N_4. The In 3d and S 2p XPS spectra gave similar results (Figs. S2b and c). The decreasing of g-C_3N_4 electron density along with the increasing of AIS electron density in g-C_3N_4/AIS composite photocatalyst verified the vital electron transfer from g-C_3N_4 to AIS.

We next evaluated the photocatalytic performance of the as-prepared g-C_3N_4/AIS composites for water splitting under visible light. Fig. 3a showed the typical time course of H_2 evolution from water splitting over 70-GAIS within 24 h. The sample exhibited rapid H_2 evolution in the first 4 h, with a rate of about 962 µmol g^{-1} h^{-1}, followed by a slow H_2 evolution process until 20 h, and a prolonged irradiation time over 24 h did not result in further increasing of H_2 production. The average H_2 evolution rate in 24 h was calculated to be 237 µmol g^{-1} h^{-1} over 70-GAIS photocatalyst. The cumulative H_2 productions of various photocatalysts under visible light irradiation in 24 h were shown in Fig. 3b. Neither pristine g-C_3N_4 nor AIS had detectable photocatalytic performance for H_2 production from water splitting. However, simple deposition of AIS onto g-C_3N_4 could significantly enhance the photocatalytic activity, and this improvement was related to the added amount of g-C_3N_4 in the reaction mixture during catalyst preparation. When feeding amout of g-C_3N_4 was less 70 mg, H_2 production increased with the increase of g-C_3N_4/$AgNO_3$ ratio, and the largest H_2 production was obtained in the case of 70-GAIS with the g-C_3N_4 feeding amout of 70 mg. A further increase in feeding g-C_3N_4 would suppress the hydrogen production. This result is reasonable when we consider the fact that a moderate g-C_3N_4/$AgNO_3$ ratio is equivalent to a moderate coverage degree of AIS nanotubes on g-C_3N_4 surface.

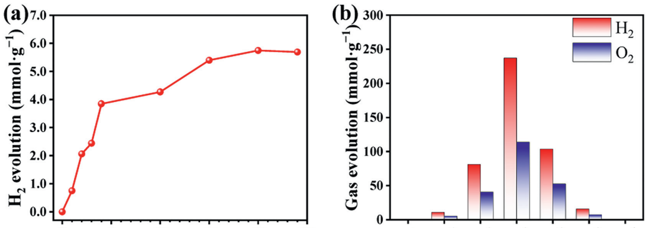

Fig. 3. (a) Typical time course of H_2 evolution from water splitting over 70-GAIS. (b) Photocatalytic water splitting performance of various photocatalysts under visible light in 24 h.

The gas products from water splitting are usually H_2 and O_2. However, no O_2 was detected in our photocatalytic water splitting experiment. According to the general splitting mechanism, we speculated that the water splitting reaction in our photocatalytic system proceeded in a two-electron pathway, *i.e.*, the oxidation product was H_2O_2. It is well-known that MnO_2 is efficient catalyst to decompose H_2O_2 into O_2 and H_2O as $2H_2O_2 \rightarrow O_2 + 2H_2O$. To verify our speculation, a certain amount of MnO_2 was added to the 70-GAIS reaction suspension after a 24-h photocatalytic reaction [31,46-47]. As shown in Fig. S3a (Supporting information), the amount of O_2 evolution gradually increased after the addition of MnO_2 and remained unchanged after 90 min. No additional H_2 evolution was detected throughout this process. The cumulative O_2 evolution within 120 min was 2.73 mmol/g, which was just half the H_2 production in a 24-h photocatalytic reaction. Regardless of the g-C_3N_4 content, an apparent 2:1 stoichiometric ratio of H_2 to O_2 was observed for all prepared g-C_3N_4/AIS photocatalysts (Fig. 3b), indicating that equimolar H_2 and H_2O_2 were produced in a typical photocatalytic water splitting reaction. This two-electron pathway for water splitting was further verified by rotating ring-disk electrode (RRDE) test. It is well known that a 0.9 V (*vs.* NHE) potential of ring electrode could ensure the generated H_2O_2 on disk electrode to be oxidized to O_2 [14,15]. The electron transfer number under this potential was 1.92 (Fig. S3b in Supporting information), indicating the crucial H_2O_2 species on disk electrode and therefore revealing a two-electron pathway of water splitting ($2H_2O \rightarrow H_2 + H_2O_2$) over g-$C_3N_4$/AIS photocatalysts. The excellent photocatalytic H_2 production performance of the optimal catalyst (70-GAIS) in this work exceeded that of most of the g-C_3N_4-based photocatalysts for simultaneous H_2 and H_2O_2 production from water splitting [15,48,49] and was comparable with that of previously reported Co_xNi_yP clusters decorated phosphorized-g-C_3N_4 photocatalyst [31].

Efficient charge separation and fast charge carrier transfer are essential to achieve satisfactory photocatalytic efficiency [50]. To disclose the interfacial charge transfer behavior, we next performed spectroscopic and photoelectrochemical studies. The steady-state photoluminescence (PL) spectra were depicted in Fig. 4a. It is obvious that g-C_3N_4 displayed intense emission at about 463 nm, which originated from the recombination of the excited electron-hole pairs [50]. AIS nanotubes gave a moderate emission band at 380−470 nm whereas for g-C_3N_4/AIS composite the photoluminescence nearly quenched within the determined wavelength range. This phenomenon indicated that recombination of photogenerated electron-hole pairs over g-C_3N_4 had been effectively inhibited after deposition of AIS nanotubes. Time-resolved transient fluorescence decay curves were also recorded to investigate the charge carrier

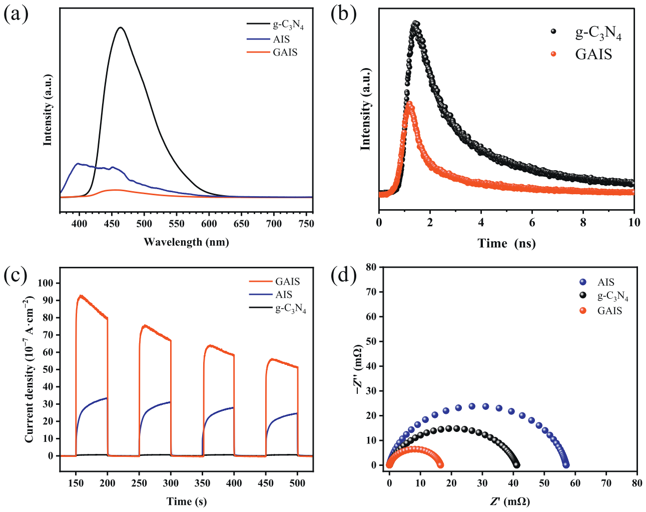

Fig. 4. Steady-state photoluminescence (PL) spectra (a), time-resolved transient fluorescence decay curves (b), photocurrent responses (c), and Nyquist plot from an electrochemical impedance spectroscopy study (d) of g-C_3N_4, AIS, and 70-GAIS.

lifetime. GAIS exhibited a relatively faster exponential decay than g-C_3N_4 (Fig. 4b). The average charge carrier lifetimes of GAIS and g-C_3N_4 were calculated to be 1.60 and 1.80 ns, respectively. This significantly declined lifetime signified faster transfer of photogenerated charge carriers on the surface/interface of GAIS photocatalyst. Such an enhanced charge transfer property was further validated by a larger photocurrent response of GAIS compared to pure g-C_3N_4 and AIS (Fig. 4c). Furthermore, electrochemical impedance spectroscopy (EIS) study also demonstrated that GAIS had the lowest interfacial charge transfer resistance, as evidenced by the smallest arc radius in corresponding Nyquist plots (Fig. 4d) [51,52].

Take all the results together, we could conclude that the strong heterojunction interaction at the interfacial region of the g-C_3N_4/AIS photocatalyst facilitated the separation and transfer of photogenerated charge carriers, and therefore achieved excellent photocatalytic performance towards water splitting.

Fig. S4 (Supporting information) displayed N_2 adsorption-desorption isotherms and the corresponding pore size distribution curves of g-C_3N_4, AIS, and GAIS. Obviously, all three materials gave typical Type IV isotherm with Type H3 hysteresis loop (Fig. S4a) according to IUPAC classification [53], indicating the mesoporous feature of these materials. The Type H3 hysteresis loop suggested that the mesoporous structures were associated with slit-shaped pores formed by aggregates of plate-like particles [53,54]. The pore size distribution curves derived from desorption isotherm branches by BJH method indicated that mesopores were deficient in AIS, whereas g-C_3N_4 and GAIS had more mesoporous structure with pore width centered at 32.5 nm (g-C_3N_4) and 3.7 nm (GAIS), respectively (Fig. S4b). g-C_3N_4 and AIS showed close BET specific surface area (19 and 21 m^2/g) and pore volume (0.11 and 0.09 cm^3/g). However, after deposition of AIS onto the g-C_3N_4 surface, the specific surface area and pore volume of the GAIS composite significantly elevated to 67 m^2/g and 0.28 cm^3/g respectively, along with a decrease of average pore size to 9.2 nm (The average pore size is 19.5 and 12.0 nm for g-C_3N_4 and AIS, respectively). This result was associated with the emerging slit-like pores in the interfacial region of g-C_3N_4/AIS. The increased specific surface area and pore volume of g-C_3N_4/AIS composite catalyst could provide more active sites for photocatalytic reaction and facilitate the escape of gaseous products.

In the following experiments, $AgNO_3$ and $Pb(NO_3)_2$ were employed as indicators to analyze the active sites for reduction and oxidation in a photocatalytic water splitting system. As shown in Figs. 5a and b, Ag particles were deposited on the surface of g-C_3N_4 nanosheets, and clear lattice spacings of 0.23 and 0.32 nm are in good agreement with the (111) lattice planes of Ag and (002) planes of g-C_3N_4 [13,55], respectively. It turned out that the reduction active sites are located on the g-C_3N_4 surface in the process of photocatalytic water splitting. The clear lattice spacings of 0.28 and 0.31 nm in Fig. 5d correspond to (111) planes of PbO_2 and (201) planes of $AgInS_2$ respectively [13,38], where PbO_2 particles were deposited on the surface of AIS nanotubes (Fig. 5c). This result suggested that the oxidation sites are located on the surface of AIS nanotubes.

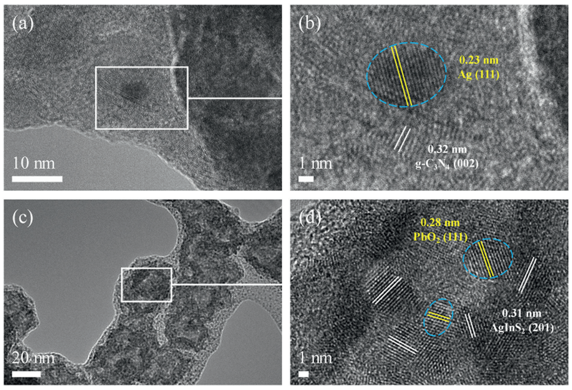

Fig. 5. HRTEM micrographs of reduction sites (a, b) and oxidation sites (c, d) over 70-GAIS.

The photoelectrochemical properties and the electron band structures of photocatalysts were further investigated by UV–vis diffuse reflectance spectroscopy (DRS) analysis. As can be seen from Fig. 6a, g-C_3N_4 could absorb light from ultraviolet to visible region with an absorption edge at about 465 nm. AIS nanotubes could capture photons in the whole UV–vis region with an absorption edge up to 784 nm, although its absorption intensity was relatively weaker than that of g-C_3N_4. After deposition of AIS onto g-C_3N_4, the GAIS composite exhibited excellent visible absorption property with an absorption edge up to 758 nm and enhanced absorption intensity comparable with that of g-C_3N_4. The band gap (E_g) of such photocatalysts were determined using Tauc plot analysis as described in Fig. 6b. The E_g of g-C_3N_4 and AIS were calculated to be 2.78 and 2.49 eV, respectively. The significantly decreased band gap of GAIS contributed to its excellent visible absorption performance. In addition, the flat band potentials of g-C_3N_4 and AIS were determined by Mott-Schottky plot. As shown in Fig. 6c, the positive slopes for both g-C_3N_4 and AIS indicated their n-type semiconductor nature [56]. The flat potentials (V_{FB}) of g-C_3N_4 and AIS were determined to be −1.52 and −0.72 V (*vs.* NHE, normal hydrogen electrode), respectively. Therefore, the corresponding conduction band minima (V_{CB}) were calculated to be −1.32 and −0.52 V (*vs.* NHE) for g-C_3N_4 and AIS, respectively. The valence band maxima (V_{VB}) can thus be calculated as +1.46 and +1.97 eV for g-C_3N_4 and AIS, respectively.

Based on all experimental results, a possible photocatalytic water splitting mechanism for simultaneous production of H_2 and H_2O_2 was proposed in Fig. 6d. Under visible irradiation, electrons located in the valance bands (VB) of g-C_3N_4 and AIS are respectively photoexcited to their conduction bands (CB), forming electron-hole pairs ($e^-{-}h^+$). Since low energy gap and intimate contact in interfacial region, photogenerated electrons on the CB of AIS can easily combinate with holes on the VB of g-C_3N_4, remaining high-reactive photogenerated electrons on the CB of g-C_3N_4 and holes on the VB of AIS. Subsequently, the high-reactive carriers migrate to the surface of the photocatalyst to produce ac-

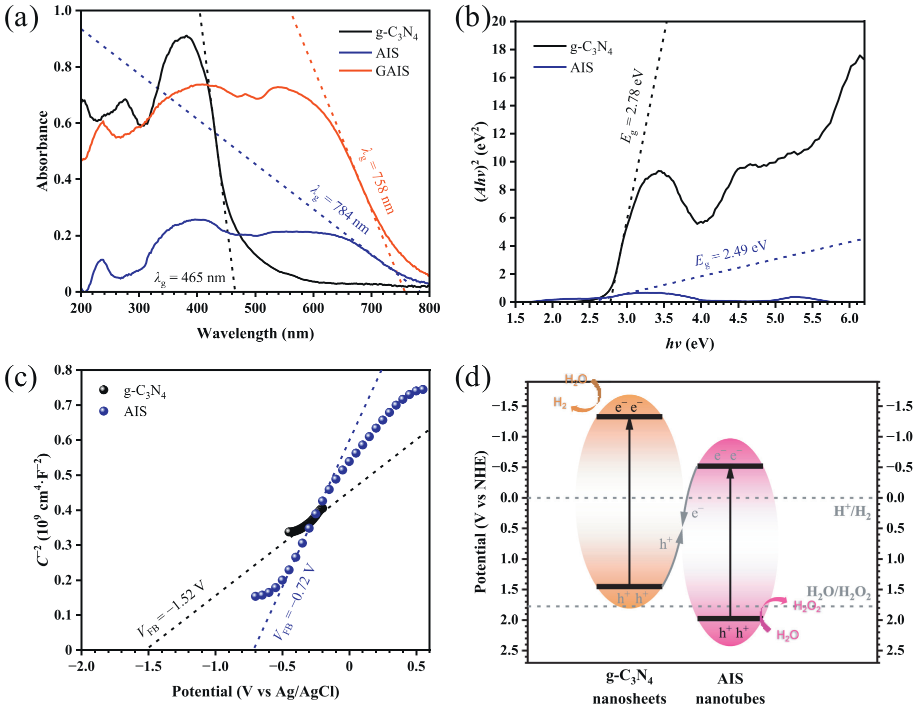

Fig. 6. (a) UV–vis diffuse reflectance spectra, and (b) Tauc plots of g-C_3N_4, AIS, and 70-GAIS, where *A* refers to the absorbance. (c) Mott-Schottky plots of g-C_3N_4 and AIS. (d) A simplified band structure diagram of g-C_3N_4/AIS photocatalyst and proposed photocatalytic mechanism for simultaneous production of H_2 and H_2O_2 from pure water splitting.

tive sites to catalyze the water splitting reaction. Owing to suitable redox potentials, the electrons on the CB of g-C_3N_4 can reduce the adsorbed H_2O to produce H_2. Meanwhile, the holes on the VB of AIS will oxidize H_2O into H_2O_2 through a two-electron pathway. Such a redox mediator-free S-scheme heterojunction photocatalyst and resultant efficient transfer, separation and migration of electrons and holes between g-C_3N_4 and AIS can inhibit the rapid recombination of highly-active photogenerated carriers, and thus the photocatalytic performance of the g-C_3N_4/AIS composite is remarkably improved.

In summary, we have successfully demonstrated a S-scheme heterojunction photocatalyst for pure water splitting into stoichiometric H_2 and H_2O_2 under visible light. The catalyst is composed of $AgIn_xS_y$ nanotubes deposited on g-C_3N_4 nanosheets prepared by classic thermal polycondensation method followed by simple coprecipitation process. The introduction of bimetallic sulfide endowed the composite catalyst with enhanced visible-light response. A suitable band alignment of g-C_3N_4/$AgIn_xS_y$ photocatalyst well meet the thermodynamic demands for simultaneous H_2 and H_2O_2 production. Therefore, excellent photocatalytic water splitting performance under visible irradiation ($\lambda > 420$ nm) can be obtained, with a 24-h H_2 evolution rate as high as 237 μmol g^{-1} h^{-1}. H_2O_2 was the only oxidation product from water splitting and produced at a 1:1 stoichiometric ratio to H_2. As a novel 3D-on-2D composite system, the g-C_3N_4/$AgIn_xS_y$ photocatalyst could provide abundant contact interface for heterojunction formation and thus efficient transfer and separation of photogenerated carriers. Water was reduced to H_2 by active e^- on the conduction band of g-C_3N_4 nanosheets and oxidized to H_2O_2 by active h^+ on the valance band of $AgIn_xS_y$ nanotubes. The efficient separation of photogenerated carriers inhibited their recombination and therefore significantly improved the photocatalytic performance. The novel 3D-on-2D configuration for heterojunction construction proposed in this work provided alternative research ideas toward photocatalytic reaction.

Declaration of competing interest

The authors declare that they have no known competing financial interests or personal relationships that could have appeared to influence the work reported in this paper.

CRediT authorship contribution statement

Hualin Jiang: Supervision. **Wenxi Ye:** Investigation. **Huitao Zhen:** Investigation. **Xubiao Luo:** Resources. **Vyacheslav Fominski:** Resources. **Long Ye:** Writing – original draft. **Pinghua Chen:** Funding acquisition.

Acknowledgments

This work is financially supported by the National Natural Science Foundation of China (Nos. 52362012, 42077162, 51978323), Natural Science Foundation of Jiangxi Province (No. 2022ACB203014), Major Discipline Academic and Technical Leaders Training Program of Jiangxi Province (Nos. 20213BCJ22018, 20232BCJ22048), Natural Science Project of the Educational Department in Jiangxi Province (No. GJJ2201121), Natural Science Foundation of Nanchang Hangkong University (No. EA202202256), Educational Reform Project of Jiangxi Province (No. JXYJG-2022–135), Nanchang Hangkong University Educational Reform Project (Nos. sz2214, sz2213, JY22017, KCPY1806).

Supplementary materials

Supplementary material associated with this article can be found, in the online version, at doi:10.1016/j.cclet.2024.109984.

References

[1] Y. Liu, X.W. Zhang, L.S. Lu, et al., Chin. Chem. Lett. 33 (2022) 1271–1274.
[2] S.S. Chen, T. Takata, K. Domen, Nat. Rev. Mater. 2 (2017) 17050.

[3] C. He, F.S. Han, W.X. Zhang, Chin. Chem. Lett. 33 (2022) 404–409.
[4] Y.M. He, D.W. Wang, Chem 4 (2018) 405–408.
[5] Z. Wang, C. Li, K. Domen, Chem. Soc. Rev. 48 (2019) 2109–2125.
[6] B.A. Pinaud, J.D. Benck, L.C. Seitz, et al., Energy Environ. Sci. 6 (2013) 1983–2002.
[7] D.M. Fabian, S. Hu, N. Singh, et al., Energy Environ. Sci. 8 (2015) 2825–2850.
[8] Y. Goto, T. Hisatomi, Q. Wang, et al., Joule 2 (2018) 509–520.
[9] Z. Wang, Y. Inoue, T. Hisatomi, et al., Nat. Catal. 1 (2018) 756–763.
[10] F.A. Chowdhury, M.L. Trudeau, H. Guo, et al., Nat. Commun. 9 (2018) 1707.
[11] Y. Qi, Y. Zhao, Y.Y. Gao, et al., Joule 2 (2018) 2393–2402.
[12] A. Kudo, Y. Miseki, Chem. Soc. Rev. 38 (2009) 253–278.
[13] X.Q. Wu, C. Zhu, L.P. Wang, et al., ACS Catal. 7 (2017) 1637–1645.
[14] Z. Li, C. Kong, G.X. Lu, J. Phys. Chem. C 120 (2016) 56–63.
[15] J. Liu, Y. Liu, N.Y. Liu, et al., Science 347 (2015) 970–974.
[16] J.Y. Tang, T.S. Zhao, D. Solanki, et al., Joule 5 (2021) 1432–1461.
[17] Y.Y. Sun, L. Han, P. Strasser, Chem. Soc. Rev. 49 (2020) 6605–6631.
[18] S. Nakabayashi, A. Fujishima, K. Honda, Chem. Phys. Lett. 102 (1983) 464–465.
[19] R. Baba, S. Nakabayashi, A. Fujishima, et al., J. Phys. Chem. C 89 (1985) 1902–1905.
[20] X.C. Wang, K. Maeda, A. Thomas, et al., Nat. Mater. 8 (2009) 76–80.
[21] G.G. Zhang, Z.A. Lan, X.C. Wang, Chem. Sci. 8 (2017) 5261–5274.
[22] C. Cheng, L.H. Mao, J.W. Shi, et al., J. Mater. Chem. A 9 (2021) 12299–12306.
[23] P. Qiu, Y. An, X. Wang, et al., Chin. Chem. Lett. 34 (2023) 108246.
[24] B. Sun, S. Lu, Y. Qian, et al., Carbon Energy 5 (2023) e305.
[25] B. Fang, Z. Xing, D. Sun, et al., Adv. Powder Technol. 1 (2022) 100021.
[26] W. Liu, L.L. Cao, W.R. Cheng, et al., Angew. Chem. Int. Ed. 56 (2017) 9312–9317.
[27] Z.M. Pan, Y. Zheng, F.S. Guo, et al., ChemSusChem 10 (2017) 87–90.
[28] F. Guo, W.L. Shi, C. Zhu, et al., Appl. Catal. B l 226 (2018) 412–420.
[29] C. Cheng, J.W. Shi, L.Y. Wen, et al., Carbon 181 (2021) 193–203.
[30] F. Xue, Y.T. Si, C. Cheng, et al., Nano Energy 103 (2022) 107799.
[31] F. Xue, Y.T. Si, M. Wang, et al., Nano Energy 62 (2019) 823–831.
[32] P.X. Qiu, C.M. Xu, N. Zhou, et al., Appl. Catal. B 221 (2018) 27–35.
[33] C.M. Li, D.Q. Zhu, S.S. Cheng, et al., Chin. Chem. Lett. 33 (2022) 1141–1153.
[34] K. Wu, L. Mao, X.Q. Gu, et al., Chin. Chem. Lett. 33 (2022) 926–929.
[35] M. Kruszynska, H. Borchert, J. Parisi, et al., J. Am. Chem. Soc. 132 (2010) 15976–15986.
[36] S.T. Connor, C.M. Hsu, B.D. Weil, et al., J. Am. Chem. Soc. 131 (2009) 4962–4966.
[37] X.B. Hu, T. Chen, Y.Q. Xu, et al., J. Lumin. 200 (2018) 189–195.
[38] W.J. Zhang, D.Z. Li, Z.X. Chen, et al., Mater. Res. Bull. 46 (2011) 975–982.
[39] Y.B. Jiang, Z.Z. Sun, C. Tang, et al., Appl. Catal. B 240 (2019) 30–38.
[40] G. Liu, S. Yan, L. Shi, et al., Front. Chem. 7 (2019) 639.
[41] H.J. Kong, D.H. Won, J. Kim, et al., Chem. Mater. 28 (2016) 1318–1324.
[42] J.W. Fu, Q.L. Xu, J.X. Low, et al., Appl. Catal. B 243 (2019) 556–565.
[43] Y.Z. Hong, Y.H. Jiang, C.S. Li, et al., Appl. Catal. B 180 (2016) 663–673.
[44] S.N. Cui, Z.Q. Ye, C. Qian, et al., J. Mater. Sci. Mater. Electron. 29 (2018) 15138–15146.
[45] X.Q. Li, Y.M. Shi, P.H. Chen, et al., J. Chem. Technol. Biotechnol. 94 (2019) 3713–3724.
[46] Q. Tian, X.K. Zeng, C. Zhao, et al., Adv. Funct. Mater. 33 (2023) 2213173.
[47] Q. Zhu, J. Wu, M. Du, et al., Photomat (2023) 1–20.
[48] Y.J. Fu, C.A. Liu, M.L. Zhang, et al., Adv. Energy Mater. 8 (2018) 1802525.
[49] J. Liu, N.Y. Liu, H. Li, et al., Nanoscale 8 (2016) 11956–11961.
[50] B. Yan, Z.H. Chen, Y.X. Xu, Chem. Asian J. 15 (2020) 2329–2340.
[51] J. Wang, G.H. Wang, X. Wang, et al., Carbon 149 (2019) 618–626.
[52] X.X. Li, X.C. Liu, C. Liu, et al., Tungsten 5 (2023) 100–108.
[53] K.S.W. Sing, D.H. Everett, R.A.W. Haul, et al., Pure Appl. Chem. 57 (1985) 603–619.
[54] H.L. Jiang, W.B. Zhang, P.H. Chen, et al., J. Mater. Chem. A 4 (2016) 11897–11907.
[55] P.H. Chen, S.Y. Li, X.Q. Tang, et al., J. Environ. Chem. Eng. 10 (2022) 107998.
[56] F.X. Dai, Y. Wang, X.R. Zhou, et al., Appl. Surf. Sci. 517 (2020) 146161.